Journal of CO2 Utilization 89 (2024) 102962

Contents lists available at ScienceDirect

Journal of CO2 Utilization

journal homepage: www.elsevier.com/locate/jcou

Highly dispersed Ni-Ce catalyst over clay montmorillonite K10 in low-temperature CO_2 methanation

Francesco Nocito [a,b,d], Nicoletta Ditaranto [a,c,d], Angela Dibenedetto [a,b,d,*]

[a] Department of Chemistry, University of Bari Aldo Moro, via E. Orabona 4, Bari 70125, Italy
[b] CIRCC, Interuniversity Consortium on Chemical Reactivity and Catalysis, Bari Unit, via C. Ulpiani, Bari 70126, Italy
[c] CSGI, Center for Colloid and Surface Science, Bari Unit, via E. Orabona 4, Bari 70125, Italy
[d] METEA Research Center, via C. Ulpiani 70126 Bari, Italy

ARTICLE INFO

Keywords:
Heterogeneous catalysis
Carbon dioxide methanation
Nickel-based catalyst
Surface chemistry
Cerium promoter

ABSTRACT

The Carbon Capture and Utilization (CCU) option can be an efficient solution for CO_2 emission mitigation. To this end, we have investigated the carbon dioxide methanation at low temperatures. Highly active, selective, stable, low-cost catalysts are required for energy and carbon balance benefits. Supported nickel-based catalysts result as the most studied and promising candidates showing a good compromise between performance and low preparation costs. The catalyst design role is key to obtaining the best performance, requiring many experiments and optimisation procedures. Herein, the enhanced Montmorillonite MK10-supported Ni(0)Ce(III) catalyst, prepared by consecutive hydrothermal and electrostatic adsorption methods followed by reduction under hydrogen flow, was used in batch CO_2 methanation, exhibiting 76 % of CO_2 conversion with 100 % CH_4 selectivity after 3 h. The catalytic system reveals very high robustness preserving the same activity and selectivity for at least 5 reaction cycles if compared with γ-Al_2O_3-supported Ni(0)Ce(III) catalyst, the latter showing the same activity but only in the first cycle. EDX, XPS, SEM, TPD, TPR, and BET characterisation techniques were used to elucidate and evaluate the potential synergistic effect of the active metal centre-promoter-support interfaces, highlighting their role in the activity and robustness of the catalyst, comparing the same effect using different alumina and silicate solid supports. The effects of the reaction conditions on the methane yield and selectivity were also evaluated.

1. Introduction

Atmospheric carbon dioxide mitigation is necessary to limit environmental imbalances with serious consequences for human society. It requires gradual energy matrix replacement by increasing the contribution of renewable energies [1] and the simultaneous development of progressively efficient technologies for CO_2 capture and conversion (CCU), especially towards more valuable and usable products such as fuels and chemicals [2–6]. In particular, the CO_2 methanation, also called the Sabatier reaction (Eq. (1)), being thermodynamically favoured at low temperature and room pressure, can be considered a promising process when coupled with green hydrogen production [7] for hidden Power-to-Methane effort [8], also if kinetic hindrance limits its large-scale industrial application [9].

$$CO_2 + 4H_2 \leftrightarrows CH_4 + 2H_2O \ (\Delta H^0_{298K} = -165 \text{ kJ/mol}) \quad (1)$$

Another restriction is represented by the reverse water gas shift reaction (RWGS, Eq. (2), a secondary mildly endothermic process that could occur during the methanation even favoured at low temperatures.

$$CO_2 + H_2 \leftrightarrows CO + H_2O \ (\Delta H^0_{298K} = 41 \text{ kJ/mol}) \quad (2)$$

Thus, developing highly efficient, selective, and resistant catalysts that work under mild reaction conditions can help bypass those limits. A large number of catalysts have been proposed in the literature for CO_2 methanation, especially based on expensive noble metals, e.g. Ru, Rh, Pd, and Pt [10–12], supported over mesoporous solids, displaying good activity and selectivity but with high process costs that restrict the industrial application. Among cheaper metals, nickel in the reduced state is the most attractive due to the good compromise between availability and catalytic activity [13]. It is worth mentioning that Ni-based catalysts show some stability limits that are strongly dependent on their composition and the suited reaction conditions [14], especially under high temperatures. They are often susceptible to carbon deposition and generally poisoning that can act as blocks for the catalytic active sites

* Corresponding author at: Department of Chemistry, University of Bari Aldo Moro, via E. Orabona 4, Bari 70125, Italy.
E-mail address: angela.dibenedetto@uniba.it (A. Dibenedetto).

https://doi.org/10.1016/j.jcou.2024.102962
Received 29 August 2024; Received in revised form 4 October 2024; Accepted 12 October 2024
Available online 17 October 2024

[15,16]. The high sensitivity to metal sintering which produces larger particle sizes with a further decrease of the active surface area is also important to consider [17]. As reported in the literature, for the carbon dioxide methanation over Ni-based catalyst, the reaction efficiency and the catalyst robustness are strongly influenced by different parameters, such as Ni loading affecting the active metal particle size and consequently the methane selectivity [18], the presence of a promoter that can increase the catalyst-CO_2 interaction [19,20] and the nature of the support, crucial for the metal dispersion and catalyst stability [21]. In some cases, also the adopted catalyst synthetic procedure can affect the efficiency and stability as observed by comparing the finely dispersed Ni nanoparticles deposited on the surface of SiO_2 via strong electrostatic interaction [22] and the use of a stabilizing agent during the nickel particles dispersion [23]. In the present paper, we used the Strong Electrostatic Adsorption (SEA) that exploits only the strong interaction between metal and support permitting highly dispersed and ultrasmall metal centre particles. Generally, increasing the nickel amount on the support increases the catalyst activity but negatively affects the metal reducibility and durability [24]. Working on the type of support, its function, and the catalyst synthetic procedure, the right combination to obtain a long-life catalyst should be the active metal amount and its distribution on the support. Many studies have been reported on the use of Ni-based catalysts over different supports, mainly based on aluminates or silicates [24–26], but also CeO_2 [27], in the presence or absence of a promoter [28,29]. As already reported in the literature, the use of cerium oxide as a support or promoter can positively affect the catalyst efficiency for different reasons. Alarcòn et al. demonstrate that improves the nickel reductive ability and increases the catalyst basicity [30], Zhou et al. highlighted the enhancement of catalyst thermal stability [31] and Liu reports on the effect on the Ni interaction with Al_2O_3 [32]. Nevertheless, only a few examples have been reported comparing the support/promoter/active center potential synergistic effects using different aluminate and silicate-derived solid supports, correlating their textural and surface properties with activity and robustness [33–35]. In this paper, we report on the preparation by the Strong Electrostatic Adsorption method of a very active and robust highly dispersed Ce(III) promoted Ni(0) catalyst supported over clay Montmorillonite K10 and its application in the low-temperature carbon dioxide methanation, in batch conditions. Montmorillonite K10 is a cheap 2:1 layer structured alumino-silicate mineral with an ideal formula of $[(Al_{3.50–2.80}Mg_{0.50–1.20})\ (Si_8)O_{20}(OH)_4]Na_{0.50–1.20}$ [36], consisting of a dominantly Al–OH octahedral sheet sandwiched by two Si–O tetrahedral sheets. Its composition and characteristic layered structure make it suitable as support in CO_2 methanation. It exhibits specific properties such as acidity, ion-exchange features, versatility, and easy recoverability [37]. The methanation reactions were performed in the batch reactor to easily examine the effects of CO_2/H_2 partial pressure, catalyst amount, reaction time, and temperature with the catalyst activity. Different analytical techniques, such as X-ray Photoelectron Spectroscopy (XPS), Energy Dispersive X-ray fluorescence (XRF), Scanning Electron Microscopy (SEM), Temperature Programmed Reduction and Desorption (TPR and TPD), low-temperature nitrogen adsorption/desorption (BET and pore volume measurements) were used to investigate and compare the properties of the catalyst changing the supports.

2. Experimental

2.1. Materials and methods

Titanosilicate TS-1 and hydrotalcite (HDL) were prepared according to the method described by Clerici et al. [38] and Perrone et al. [39] respectively. Montmorillonite K10 (MK10), was purchased by Fluka. Nickel(II) dinitrate hexahydrate $Ni(NO_3)_2{\cdot}6H_2O$ 99.999 % trace metals basis, Ammonium cerium(IV) nitrate $(NH_4)_2Ce(NO_3)_6$ ≥98.5 % (by titration), Gamma alumina powder (γ-Al_2O_3) (max particle size 0.1 micron, 99.99 %) were purchased by Sigma Aldrich. High purity CO_2 was withdrawn directly from a cylinder supplied by SOL and high pure Hydrogen was produced by DBS Hydrogen generator NMH_2 250. Methane (2.5 of purity) used for the calibration curve, was purchased by Nippon Gases.

2.2. Analytical methods

Quantitative determinations on the reaction solutions were performed using a Thermo-Fisher gas-chromatograph (TCD-GC) equipped with a Supelco Carboxen 1010 Plot capillary column. Catalyst surface characterisation (BET, acid/basic sites, total pore volume, TPD and TPR) was done using Pulse Chemisorb 2750 (Micromeritics) instrument equipped with a Thermal Conductivity Detector (TCD). Bulk elemental analyses (XRF) of all materials were performed using a Shimadzu EDX-720 Energy Dispersive X-ray Spectrometer with an X-ray tube of Rh target (5–50 kV) and Si(Li) detecting system. Scanning Electron Microscopy (SEM) analyses were performed with a ZEISS VP300 EDAX Oxford Instrument. Surface elemental and chemical speciation analysis (XPS) were performed with a Versa Probe II Scanning XPS Microprobe spectrometer (Physical Electronics GmbH) using a monochromatized AlKα source with an x-ray spot size of 200 μm and a power of 47.6 W. Wide scans and detailed spectra were acquired in Fixed Analyzer Transmission (FAT) mode with a pass energy of 117.40 eV and 46.95 eV respectively. An electron gun was used for charge compensation (1.0 V, 20.0 μA). All binding energies were referenced to C1s at 284.8±0.1 eV for adventitious hydrocarbon. Data processing was performed using MultiPak software v. 9.9.0.8, 2018.

2.3. Synthesis of catalytic materials

2.3.1. Ni-based supported catalyst preparation

To synthesize different Ni-supported catalysts and to compare the nickel-precursor/support affinity, the Strong Electrostatic Adsorption (SEA) procedure was performed using the same support/nickel-salt mass ratio under the same time of contact (the higher after which no more nickel salt can be deposited at room temperature), as following reported. Subsequently, the amounts of nickel bonded to the different supports were measured.

500 mg of $Ni(NO_3)_2{\cdot}6H_2O$ (101 mg of Ni) were dissolved in 30 mL of deionized water (the solution is emerald-colored) and added dropwise to a stirred suspension of 500 mg of support in 30 mL of deionized water (total dropping time: 30 min). The pH of the solution was kept higher than point zero charges (pzc) (only in the case of HDL was used NaOH). The obtained suspension was stirred at room temperature for 15 h and then centrifuged to separate the liquid phase. The resulting solid was washed with 2 × 3 mL of fresh deionized water and subsequently dried in a water bath at 85 °C. Finally, it was ground and calcined in air at 500 °C for 3 h. After the calcination, the sample was cooled to room temperature in a dry chamber and treated under Argon/Hydrogen mixture flow (90 %–10 %, 30 mL/min) at 600 °C for 2 h to nickel reduction.

2.3.2. Supported Ce oxide preparation

Microwave-assisted deposition was used to prepare Ce oxide-supported, reducing the deposition time and costs. To compare the affinity of the different supports with respect to cerium oxide precursor, the same support/cerium-salt mass ratio was used under the same contact time, as reported below.

110 mg of $(NH_4)_2Ce(NO_3)_6$ (28 mg of Ce), were dissolved into 10 mL of deionized water (solution appears of orange color). This solution was added drop by drop and under stirring to a suspension composed of 1000 mg of support in 35 mL of deionized water (total dropping time: 30 min) and subsequently subjected to the microwave-assisted hydrothermal process (MWA-HT), in a hermetically sealed 100 mL Teflon vessel at 110 °C for 1 h (500 W of the microwave power supply). After MWA-HT, the suspension was cooled down to room temperature, and

Table 1
Catalytic activities to evaluate the effect of time carried out at 260 °C.

Entry	Cat	CH_4 yield (%) – 1 h	CH_4 yield (%) – 3 h
1	Ni/TS1	0	0
2	Ni/HDL	30.9	31.6
3	Ni/MK10	24.2	44.2
4	Ni/Al_2O_3	41.3	53.7
5	Ni/Ce/TS1	0	1.6
6	Ni/Ce/HDL	32.6	33.1
7	Ni/Ce/MK10	61.2	76.0
8	$Ni/Ce/Al_2O_3$	63.3	78.2

the liquid phase was separated by centrifugation and siphoning. The obtained solid was washed with 2 × 3 mL of fresh deionized water, then it was dried at 85 °C. Finally, it was calcined, for 3 h, in air at 700 °C, representing the optimal temperature with the best compromise between surface area, basicity and energy consumption, as highlighted in Table S3 and already studied in our previous work [40].

2.3.3. Preparation of Ni/Ce oxide-supported catalyst

500 mg of $Ni(NO_3)_2{\cdot}6H_2O$ (101 mg of Ni) were dissolved in 30 mL of deionized water (solution is emerald colored) and added dropwise to a stirred suspension composed of 500 mg of supported Ce oxide in 30 mL of deionized water (total dropping time: 30 min). The pH of the solution was kept higher than pzc (only in the case of HDL was used NaOH). The suspension was then stirred at room temperature for 15 h and subsequently treated in a water bath at 85 °C until dry. The obtained solid was ground and calcined in air at 500 °C for 3 h. At the end of calcination, the sample was cooled down to room temperature in a dry chamber and subjected to nickel reduction under Argon/Hydrogen mixture flow (90 %–10 %, 30 mL/min) at 600 °C for 2 h.

2.4. Catalysts characterisation

All the samples were pretreated under Helium carrier flow (30 mL/min) at 450 °C for 3 h. About 200 mg of sample were used under isotherms N_2 absorption at -196 °C, followed by room temperature desorption. The specific surface area (BET) was estimated using the standard Brunauer–Emmett–Teller method. Single point adsorption at p/p0 = 0.98 was used to determine the total pore volume (Vp). Analyses of acid and basic sites were carried out using NH_3 or CO_2 as probe gas respectively. The reducibility of catalysts was determined by the Temperature Programmed Reduction (TPR) method using a 10 % H_2/Ar mixture with a flow of 25 mL/min and a temperature-increasing program of 10 °C/min. Water produced during the reduction was removed using a cold trap (liquid nitrogen and isopropyl alcohol, down to -110 °C). The TPR profiles were normalized to the amount of nickel present.

2.5. Study of the catalytic activity

The CO_2 methanation was carried out in a batch system, using a 200 mL stainless steel autoclave equipped with a manometer for inner pressure control, a glass reactor, and a sintered glass septum that permits keeping the catalyst not in contact with the base of the reactor. Before use, the autoclave was purged using vacuum and nitrogen flow cycles removing air and moisture, completely. Then, the catalyst (500 mg) was added, and the autoclave was closed and charged with CO_2/H_2 mixture (2 and 8 bar respectively). The reaction temperature was fixed using an electric jacket, and a K-type thermocouple. The system was heated and kept for the given time, as reported in Table 1. At the end of the reaction, the autoclave was cooled to room temperature and, the gaseous mixture analyzed through a TCD-GC. CO_2 conversion and CH_4 selectivity were measured using a GC calibration curve. The conversion of CO_2 (χ CO_2), and selectivity into CH_4 and CO (χ CH_4, χ CO respectively) were determined by using the following formula (mol CO_2 (in) is the number of moles of starting CO_2 in the reaction mixture; mol CO_2 (out) is the number of moles of remaining CO_2 in the post-reaction mixture, mol CH_4 and mol CO are the number of moles of produced CH_4 and CO in the post-reaction mixture):

$$\chi CO_2 = \frac{\text{mol } CO_2(\text{in}) - \text{mol } CO_2(\text{out})}{\text{mol } CO_2(\text{in})} * 100$$

$$\chi CH_4 = \frac{\text{mol } CH_4}{\text{mol } CH_4 + \text{mol CO}} * 100$$

$$\chi CO = \frac{\text{mol CO}}{\text{mol } CH_4 + \text{mol CO}} * 100$$

All analytical data are considered as the average of at least three replicates.

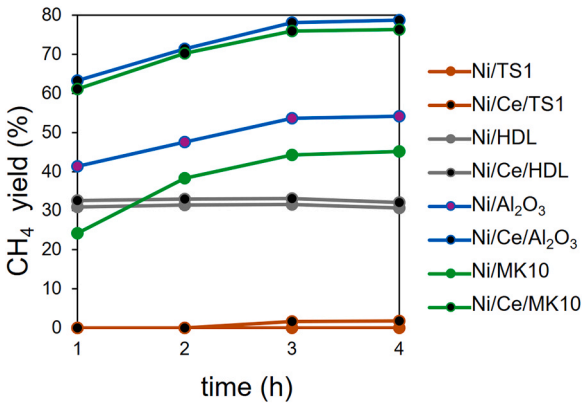

Fig. 1. CH_4 yield as a function of reaction time (pH_2/pCO_2 = 4, T=260 °C, m catalyst = 500 mg, V reactor = 200 mL).

3. Results and discussion

3.1. CO_2 methanation over different supported Ni(0) catalysts

As reported in the Experimental Section, all the catalysts were previously activated with hydrogen before their use in catalysis. Different parameter spaces were studied in the reaction to optimise the conditions and obtain higher CO_2 conversion and CH_4 selectivity under relatively low process cost.

Table 1 and Fig. 1 report the nickel catalyst's performances in the presence and absence of the promoter using 1:4 = CO_2:H_2 molar ratio at 260 °C, the lowest temperature at which 100 % of methane selectivity with high carbon dioxide conversion was achieved, carried out at different reaction times. As shown in Table 1, it appears clear that the catalytic activity was strongly dependent on the adopted support,

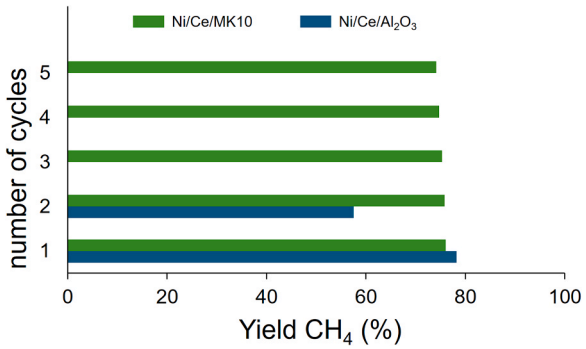

Fig. 2. CH_4 yield vs. number of cycles of reaction (t = 3 h per cycle, T = 260 °C, without catalyst reactivation).

Table 2
Surface properties and nickel content of the supports and catalysts.

Species	na $*10^{-3}$ (mmol/g)	nb $*10^{-3}$ (mmol/g)	nb/na	na/nb	S_{BET} (m^2/g)	Pore vol. (cm^3/g)	Point zero charge	Ni (% w/w) XRF	Ni (% at.) XPS	Ni (% at.) XRF	Ni dispersion (%)
TS−1	11.3	4.7	0.42	2.40	104.5	1.79	6.3	-	-	-	-
MK10	23.4	2.7	0.11	8.67	180.8	1.29	4.7	-	-	-	-
HDL	27.9	123.0	4.41	0.23	84.1	0.56	10.3	-	-	-	-
Al_2O_3	29.3	6.6	0.22	4.44	30.5	0.42	6.2	-	-	-	-
Ni/TS−1	49.7	0.8	0.02	62.1	172.4	0.88	-	2.73	2.40	5.23	28.8
Ni/MK10	8.8	4.4	0.50	2.0	274.7	0.95	-	8.37	4.40	9.88	36.5
Ni/HDL	86.3	26.0	0.30	3.32	236.0	0.53	-	2.80	5.20	4.80	22.5
Ni/Al_2O_3	116.6	52.1	0.45	2.28	65.9	0.11	-	6.24	11.10	8.33	15.4

Acid and basic sites values were measured by NH_3 and CO_2 room temperature chemisorption and TP desorption techniques respectively; the surface area was measured by low-temperature N_2 physisorption and desorption; surface nickel content was measured by XPS technique; overall nickel content was measured by EDX analysis; Point Zero Charge was measured by titration method; Ni dispersion was calculated by room temperature H_2 chemisorption.

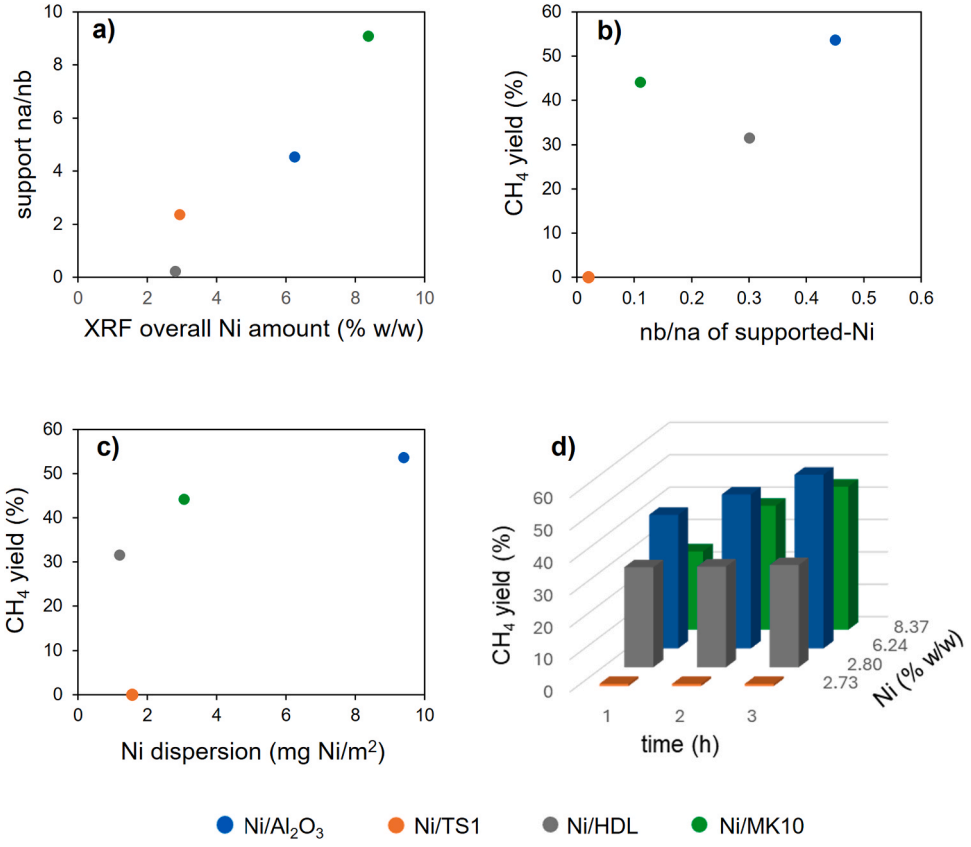

Fig. 3. Correlation between support's acidity and (a) catalyst's overall Ni content, (b) catalytic activity with catalyst basicity, and (c) Ni dispersion. (d) Effect of Ni overall amount on the catalytic activity.

resulting higher for Ni over Al_2O_3 (53.7 % of CO_2 conversion after 3 h) and practically absent under the same conditions when nickel was supported on titanosilicalite.

The effect on the catalytic activity of the addition of a small amount of Cerium oxide (<1 % w/w of cerium) as a promoter was also evaluated highlighting that an increase in methane yield was observed when Al_2O_3 and MK10 were used as support, reaching after 3 h 78.2 % and 76 % of CH_4 yield respectively. Only a slight effect was observed using HDL, while no influence was remarked on adding Ceria to the TS-1-supported catalyst. In all cases, the methane selectivity was 100 % up to 3 h of reaction. It is worth noting that Ni/Ce/Al_2O_3 and Ni/Ce/MK10 are the most active catalytic species, also if they exhibit different behavior in terms of lifetime. On both catalysts, recyclability tests were carried out to demonstrate the robustness of Ni/Ce/MK10 also without a reactivation procedure. The results shown in Fig. 2 remark that Ni/Ce/MK10 was reusable for 5 subsequent cycles (at least) maintaining almost the same activity (15 h total), while Ni/Ce/Al_2O_3 significantly decreased its activity already in the second cycle. Overlapped $Ni2p_{3/2}$ and Ce3d XP spectra of the calcined and reduced Ni/Ce/MK10 catalysts, analyzed before the reaction and after 5 cycles confirmed that the nickel and cerium oxidation states do not change , as evidenced in Fig. S1, but is the number of active sites that tend to decrease in time.

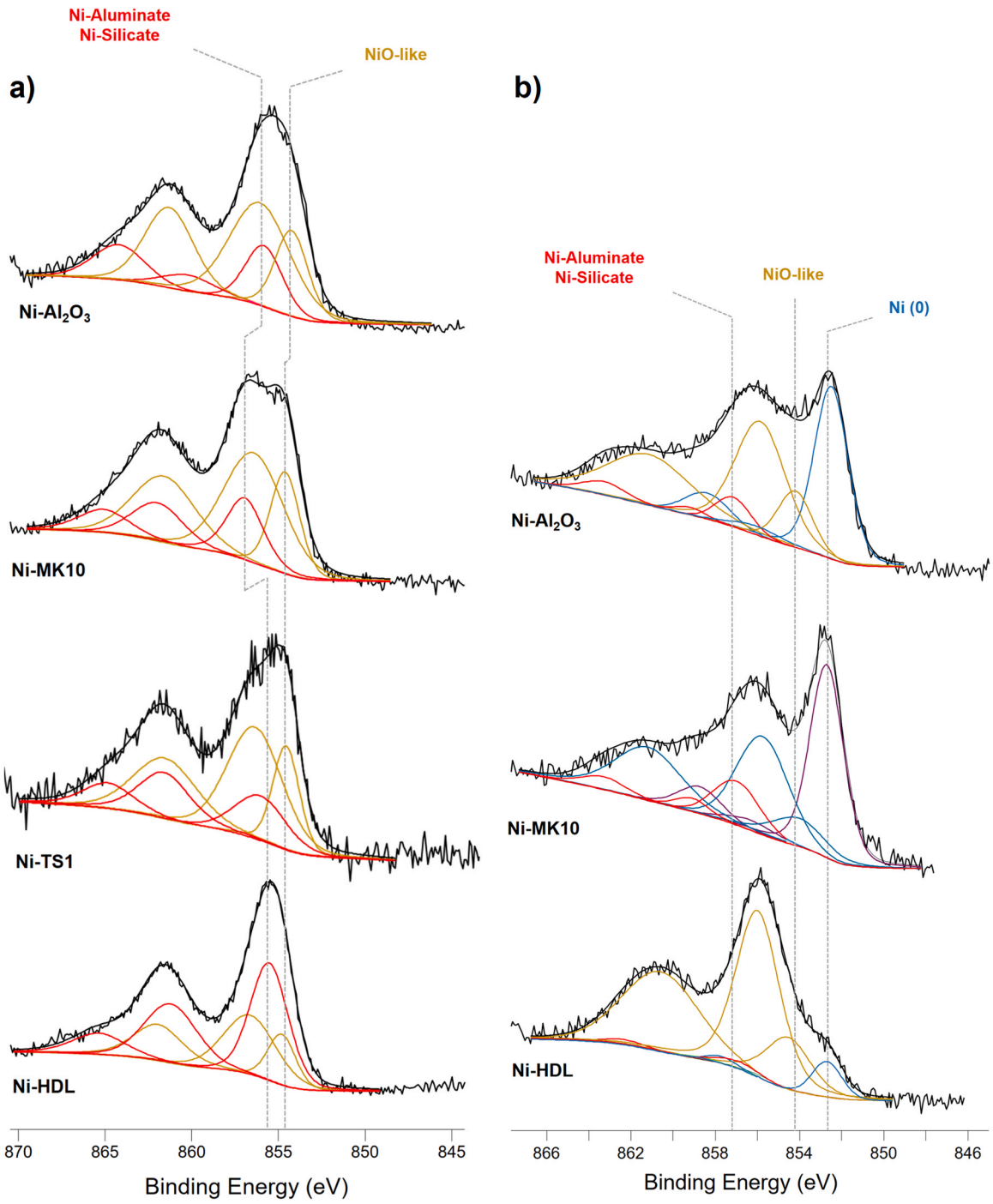

Fig. 4. Curve-fitted Ni2p$_{3/2}$ XP spectra of (a) calcined and (b) reduced Ni-catalysts. The multiplet splitting of the different Ni surface species is identified in the color code.

3.2. Studies on textural and surface properties of supported-Ni catalysts in the absence of the promoter

Table 2 shows some textural properties of both fresh supports and nickel-supported. As can be noticed about fresh supports, suitably selected as alumina and silicate derivatives solids, they show different features such as acid/basic sites molar ratio (na/nb), point of zero charge, surface area, and total pore volume which result in specific effects on the catalyst design, like active metal loading, particle size, and metal reducibility that are following evaluated.

The Strong Electrostatic Adsorption (SEA) method was used to obtain ultra-small nickel particles deposited on different supports, starting from the same amount of support and nickel precursor. They were reacted under the same conditions adjusting the pH above the point of zero charge obtaining different nickel loadings (Table 2), with Ni/MK10 exposing the highest amount (8.37 % w/w) and NI/TS1 the lowest (2.73 % w/w). Examining some correlations (Fig. 3a-d), it is possible to observe that the support acidity (in terms of na/nb) increases the amount of deposited nickel (Fig. 3a), probably because of the extensive presence of $H^{\delta+}$ groups on the support that promotes the interaction with nickel cations in the aqueous medium through a cationic exchange better than a real impregnation [41], as also confirmed by the support point of zero charge. Such nickel loading, as expected, appears strongly connected with the catalytic activity (Fig. 3b)

Table 3
XPS BE values and atomic relative abundances of the different Ni species on the surface of calcined and reduced catalysts.

	Calcined catalysts				Reduced catalysts					
	NiO-like species		Ni-Aluminate, Ni-Silicate species		Ni(0)		NiO-like species		Ni-Aluminate, Ni-Silicate species	
	BE Ni2p$_{3/2}$ (eV)	rel. ab. (%)	BE Ni2p$_{3/2}$ (eV)	rel. ab. (%)	BE Ni2p$_{3/2}$ (eV)	rel. ab. (%)	BE Ni2p$_{3/2}$ (eV)	rel. ab. (%)	BE Ni2p$_{3/2}$ (eV)	rel. ab. (%)
Ni-Al_2O_3	854.1±0.1	64±3	855.8±0.1	36±3	852.1±0.1	32±5	853.8±0.2	57±2	857.3±0.1	12±5
Ni-MK10	854.6±0.1	62±1	856.4±0.2	38±2	852.7±0.1	40±4	854.2±0.2	48±8	857.1±0.1	13±4
Ni-TS1	854.7±0.1	66±2	856.3±0.1	34±3	n.d.	n.d.	n.d.	n.d.	n.d.	n.d.
Ni-HDL	854.9±0.1	39±1	855.7±0.1	61±1	852.2±0.1	10±2	854.3±0.1	81±6	857.3±0.1	–

also if, Ni/MK10 shows slower kinetics, enhancing Ni/HDL activity after one hour of reaction. Fig. 3c highlights that the best performance of the Ni/Al_2O_3 catalyst, containing the second higher amount of nickel, is probably due to the low metal dispersion on the support surface, with a negative effect on the robustness of the catalyst itself (see Fig. 1). Moreover, if the deposited Ni amount increases with the support acidity, the overall catalyst basicity plays a key role in methane formation, as expected when CO_2 is involved [42] (Fig. 3d). This explains why Ni/TS1 results inactive even if, it contains nickel.

Additionally, the effect of nickel incorporation on different supports was evaluated by BET Surface Area (SSA) and Total Pore Volume (TPV) variation after metal loading, which is generally related to the formed NiO crystallite particle size obtained during calcination. As expected, both values resulted larger for zeolitic and layered solid materials than for porous ones, following the trend γ-Al_2O_3<HDL<TS1<MK10, as shown in Table 2.

In all cases, the SSA increased, and this feature can be attributed to the simultaneous effect of calcination, which reduces the solid granulometry [43,44], and of new geometrical efforts due to NiO crystallite formation on the support surface [45,46].

On the other hand, TPV displayed an opposite behavior with a decrease after nickel loading that suggests a partial pore or interstitial space occupation. This feature is less evident in Ni/HDL and can be explained by considering that nickel was preferentially deposited on the external surface of HDL and not in the internal layers, generally prone to anionic exchange.

This evidence was supported by X-ray Photoelectron Spectroscopy (XPS) and Energy Dispersive X-ray fluorescence (XRF) used for analysing the composition of all the catalysts at different sampling depths (Table 2).

Ni/MK10 exhibits the highest nickel content, high SSA, and high TPV (274.7 m^2/g and 0.95 cm^3/g respectively) revealing that the nickel centres are present both on the surface and internally (4.4 % as detected by XPS and 9.88 % atomic abundance as observed with XRF analyses), according to a good NiO dispersion. Ni/Al_2O_3 contains less amount of nickel (6.24 % w/w) depicting as expected, low dispersion (11.1 % on the surface) because of its lower surface area (65.9 m^2/g). Considering its scarce acidity, Ni/HDL shows a lower Ni content (2.80 % w/w). Moreover, despite the layered structure and high surface area (236 m^2/g), it contains nickel mainly on the surface (5.2 % versus 4.80 % atomic abundance up to the bulk), showing a low interlayer penetration of nickel cation. Conversely, Ni/TS1 displayed Ni center, especially in the internal part. This trend is consistent with the values obtained by H_2-chemisorption (Table 2). Detailed XPS investigations on Ni chemical speciation performed before and after the reduction procedure, allowed us to gather deep information about the different interactions between the formed nickel oxide and the various supports. Specifically, high-resolution XP spectral regions were investigated, and curve-fitted to understand the possible species that occurred on the catalysts. The results are presented in Fig. 4 and Table 3. O1s XP spectra curve fitting permitted to exclude the presence of Ni-hydroxide species on all the calcined catalysts (that are typical of not complete salt precursor degradation), while the nonlinear least-squares curve fitting procedure of Ni2p$_{3/2}$ spectral regions on the same samples, allow us to identify the multiplet splitting of two different Ni chemical environments [47] (Fig. 4a). Based on the BE values and the relative intensities of the satellites and the main peak, they were ascribed to NiO-like and Ni-Aluminate or Ni-Silicate-like species (Table 3), in agreement with what was previously reported about Ni interaction with silica- and alumina-supported catalysts [48–51].

As displayed in Table 3, calcined Ni/Al_2O_3, Ni/MK10, and Ni/TS1 show the highest content of NiO-like species, while Ni/HDL is the lowest. Despite this peak component identifying a weaker bonded Ni^{2+} chemical environment, the BE value increase from Ni/Al_2O_3 to Ni/HDL suggests an increasing interaction as the environment becomes more electronegative. Moreover, the BE value relative to the second Ni component, less weakly bonded to support than NiO-like species and ascribable to both Ni-Aluminate and/or Ni-Silicate species does not follow the same trend but, it results in almost the same for alumina-containing supports (Ni/Al_2O_3, Ni/HDL) and higher for silica- and aluminosilicate-based one (Ni/TS1, Ni/MK10).

These findings could be explained considering the well-known behavior of Ni that interacts with aluminate- and silicate-containing support diversely, resulting in nickel species occupying different sites [48]. Hercules et al. demonstrated that nickel species weakly interacting with support are thought to be located in octahedral sites and are easier to reduce than Ni located in tetrahedral sites, exhibiting a higher binding energy [48]. So, according to previously reported in the literature [50,51], the Ni component at BE=856.4±0.2 eV obtained in Ni/MK10 results compatible with Ni-(tetrahedral)silicate interaction (it should be noted that Ni-(octahedral)aluminate signal if present, would be eclipsed). A further confirmation arises from the BE values of Al2p and O1s peak components. In the Ni/MK10 catalyst, Al2p signal is shifted towards lower values (74.7±0.2 eV) with respect to bare MK10 (75.3 ±0.1 eV) highlighting an interaction with nickel; at the same time, the O1s signal presents the first peak at BE=532.7±0.1 eV, typical of aluminosilicate species, and a second peak at BE=530.6±0.2 eV (here called Oox), when Ni is supported. The latter is at higher energy than O-Ni of bulk oxide and therefore suggests a more electronegative chemical environment due to interaction with the silicate moiety of MK10 support. This O1s peak component has also been observed in Ni/TS1 catalyst, demonstrating that it is unequivocally due to Si–O–Ni interactions (see Fig. S2 and Table S1 for Ni to Oox ratio). This finding is in line with the penetration of nickel not only in the MK10 internal layers but, also, in its aluminosilicate structure, affording a better nickel dispersion.

3.3. Reducibility of Ni-supported catalysts in the absence of promoter

The "NiO species" reducibility in the Ni-supported catalysts depends on its interaction with support. This is mainly due to its arrangement on the support structure after calcination, producing particles with different sizes and dispersion [52]. In principle, a higher reduction temperature would be expected for highly stabilized nickel species and generally, three kinds of reducible NiO species can be revealed, namely α (300–550 °C), β (550–700 °C), and γ (> 700 °C) [53]. Linear

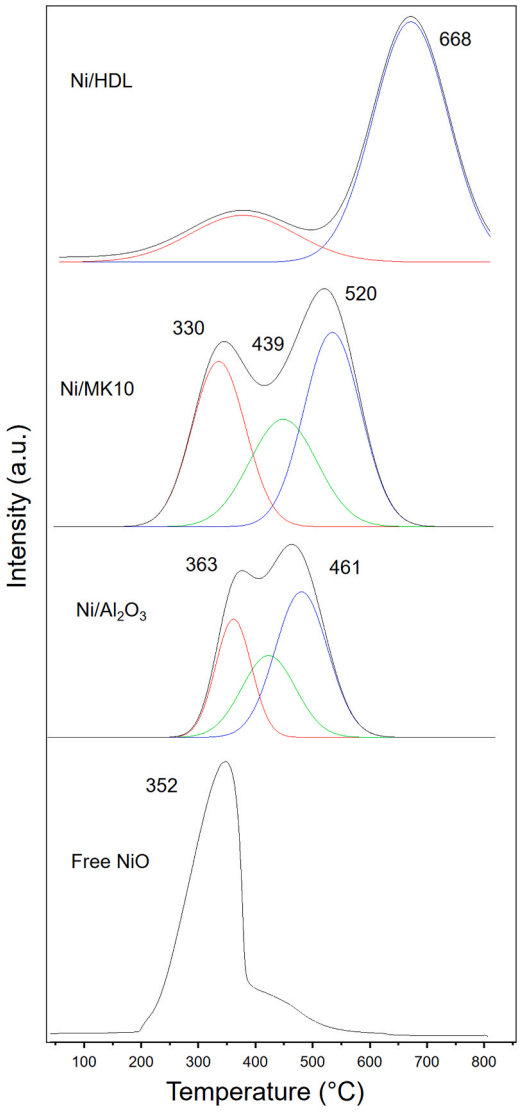

Fig. 5. TPR profiles of free nickel oxide and supported NiO.

temperature-programmed reduction H_2-TPR was carried out to analyze the reduction of the NiO species dispersed on different aluminate or alumino-silicate supports (Ni/TS1 was excluded in such investigations considering its low catalytic activity). The TPR profiles of samples calcined at 550 °C are shown in Fig. 5 and they were deconvoluted applying Gaussian-type deconvolution. The "free NiO" curve was included for comparison whilst bare supports showed no reduction peaks in the studied temperature range, as reported in the literature [54]. The complete reduction of nickel-based catalyst is achieved by increasing the temperature up to 800 °C. This was confirmed by TPR analysis carried out on the reduced catalyst. The "free Ni oxide" TPR profile shows a maximum peak at 352 °C [55]. Ni/MK10 and Ni/Al_2O_3 TPR curves present three deconvoluted reduction peaks, all with the maximum in the α-type range. In particular, Ni/MK10 shows the first at a temperature lower than that of "free NiO" (330 °C) assigned to NiO crystallite surrounded by electron-rich species that attributes a spillover effect that improves the reducibility promoting the reaction with hydrogen; a second peak at 439 °C relative to the reduction of Ni^{2+} species positioned in the octahedral alumina sites (the only one present in the MK10) and a third at 520 °C for Ni^{2+} interacted with silicates.

Ni/Al_2O_3 shows the first peak at 363 °C similar to those displayed by "free NiO" and assigned to NiO crystallite reduction exhibiting a minimal interaction with support and two reduction peaks at 439 and 461 °C relative to Ni^{2+} interacting with alumina octahedral and tetrahedral sites respectively, in line with our XPS results on the calcined samples and with what was reported by Molina et al. [56].

The Ni/HDL conversely exhibits mainly a single and broad peak in the zone of β and γ-type, typical of strong interaction with support NiO and $NiAl_2O_4$ spinels [57].

TPR experimental findings were compared and corroborated by XPS measurements. After the reduction process, a further chemical environment was ascertained in Ni2$p_{3/2}$ XP spectra of all the catalysts (Fig. 4b); it was attributed to Ni(0) species that show different abundance depending on the support (see Table 3 for BE, peak components attribution, and relative abundances). Considering both data from XP spectra and relative abundances of calcined and reduced samples reported in Table 3, it is evident that changing the support resulted in a different distribution of Ni species leading to various amounts of reduced nickel. Our experimental results agree with what is reported in the literature where the higher the NiO-like species abundance, the higher the Ni reducibility [48]. In addition, Ni/HDL yielded the lowest amount of Ni(0) due to both the lowest NiO-like abundance and its highest BE value. This behavior, in line with what was reported by Hurst et al. [58], confirms the strong correlation between the support composition and structure, the nickel loading, its dispersion, and specific interactions with support, with consequent effects on the reducibility and therefore on the catalytic activity. Generally, the reduction of a homogeneously supported metal oxide proceeds through nucleation with the reduction of individual metal ions followed by surface diffusion. Such a process may be hindered by strong metal/support interaction reducing the mobility of metal ions.

Table 4
XRF and XPS cerium elemental analysis for different Ce/support species.

Entry	Species	Ce (% w/w) XRF	Ce (% at.) XPS
1	Ce/MK10	0.66	3.5
2	Ce/HDL	0.65	0.2
3	Ce/Al_2O_3	0.50	1.1

3.4. Effect of the promoter on the activity, reducibility, and basicity of catalysts

Both CO_2 conversion and, CH_4 selectivity can be affected by the presence of promoters in the catalyst [59–61], which improve textural features and surface properties playing as electron modifiers, especially in the CO_2 chemisorption [62]. Cerium oxide exhibits this behavior, and although it is not particularly cheap, it was widely used directly as a support due to its high oxygen storage capacity and large oxygen mobility resulting from the rich defect chemistry [63–67] that increases the CO_2 interaction. In this work, it was used in a low amount as a promoter (less than 1 % w/w of Ce, see Table 4) [68] and the obtained Ce-loaded supports were subsequently interacted with nickel salt by SEA to afford, after calcination and reduction, the Ni(0)/Ce_xO_y/support materials tested as catalysts under different reaction conditions and compared with not promoted nickel species.

Also, the cerium oxide/supports affinity were evaluated, through XRF and XPS analysis, measuring the overall and surface cerium loading. The SEA method, used under microwave-assisted conditions, permitted the loading on the support, after only 1 h of treatment, of the maximum amount of cerium. As reported in Table 4, the cerium amount was practically the same in the case of HDL and MK10 (0.65 % and 0.66 % w/w respectively) and slightly less in the Al_2O_3 (0.50 % w/w). Concerning the surface atomic abundance (XPS measurement) the trend is: Ce/HDL<Ce/Al_2O_3<Ce/MK10. XPS investigations on the same samples show that cerium dispersion on the two-layered structures appears completely different. This was not true for the porous alumina for which the deposition occurs only on the surface. A preferential cerium presence

Table 5
Surface properties and nickel and cerium content of the catalysts.

Entry	Species	na $*10^{-3}$ (mmol/g)	nb $*10^{-3}$ (mmol/g)	nb/na	S_{BET} (m^2/g)	Pore vol. (cm^3/g)	Ni (% w/w) XRF	Ni (% at.) XPS	Ce (% w/w) XRF	Ce (% at.) XPS
1	Ni/Ce/MK10	1.9	4.9	2.60	99.5	2.28	1.97	1.8	0.40	2.5
2	Ni/Ce/HDL	31.5	66.5	2.11	78.2	0.39	1.40	2.7	0.48	0.6
3	Ni/Ce/Al_2O_3	41.6	3.6	0.08	20.1	0.08	0.40	10.4	0.14	1.3

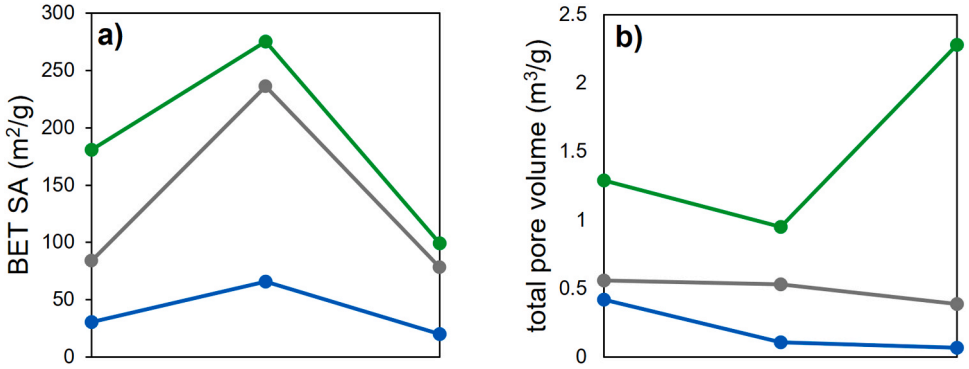

Fig. 6. Comparison between BET surface area (a) and TPV trend (b). In the sequence from left to right: support, Ni/support, and Ni/Ce/support species. Blue line for Al_2O_3, grey line for HDL and green line for MK10 support.

in the internal layers was observed for the hydrotalcite support, probably because of its anion exchanger ability [69] in which $[Ce(NO_3)_6]^{2-}$ complex intercalation was promoted by microwave treatment. This finding is in accordance with its slight increase in the catalytic activity observed after the cerium oxide loading because, conversely, nickel was preferentially deposited on the external surface, limiting their potential synergistic effect. In the case of MK10, cerium appears homogeneously located on the surface and between layers as observed for nickel. Moreover, looking at the BE position for the $Ce3d_{5/2}$ main peak, it was shifted towards higher energies than bulk CeO_2 for both the calcined Ce/Al_2O_3 (882.9±0.1 eV) and Ce/MK10 (883.5±0.1 eV), with a more evident shift for the latter, meaning a more intense Ce-support interaction. In addition, it can be highlighted the dissimilar cerium-alumina interaction mode, revealing two different cerium chemical environments on Ce/Al_2O_3, and almost exclusively CeO_2 on Ce/MK10 (u and v refer to the $3d_{3/2}$ and $3d_{5/2}$ spin-orbit components, u''' and v'' for Ce^{+4}, v' for Ce^{3+}) (see Fig. S3). Table 5 reports the Ni and Ce elemental analysis and some surface properties of the studied catalysts.

Considering data reported in Tables 2 and 5 it can be observed that for all the tested catalysts, the BET surface area variation follows a similar trend changing the support (Fig. 6a), with an increase when only nickel was added and a decrease when cerium and nickel were deposited, indicating that the formed crystallites size are very similar on all supports, in accordance with SEM analysis.

Moreover, different behaviors have been observed considering the Total Pore Volume variation trends (Fig. 6b). When Al_2O_3 was used as support (lowest TPV value), both nickel oxide and cerium oxide were deposited on the surface covering most of the pores (not sensitive differences are shown adding only nickel or both cerium and nickel consecutively).

When HDL was used as support, no decrease of TPV was measured after nickel deposition and only a modest decline when cerium and nickel were deposited, highlighting that a preferential deposition of the two metals in different areas of the support occurs (the cerium oxide shows a slightly larger effect due to both its favoured interlayer deposition and to its larger pore size if compared to nickel oxide crystallites).

A different behavior was observed by using MK10 as support. In the Ni/Ce/MK10 catalyst, to a decreasing value of SBET, obtained for the partial interlayer occlusion especially due to the cerium oxide crystallites, a simultaneous increase of TPV was measured as a consequence of a probable widening of the interlayer distance [70] and in accordance with the Wheeler's equation d(nm)=4000*V(mL/g)/S(m^2/g), suggesting a better distribution of both metals along the support. SEM analysis (Fig. 7a-c) of calcined catalysts was carried out to understand the morphological features of the materials.

The SEM images confirm the different NiO distributions over the three supports: in Fig. 7a is evident the NiO coverage on the Al_2O_3 support surface in which cerium oxide cannot be distinguished; Fig. 7b shows the bigger crystallites of cerium oxide over which little crystallite of NiO are positioned and in Fig. 7c are evident only spot crystallites of

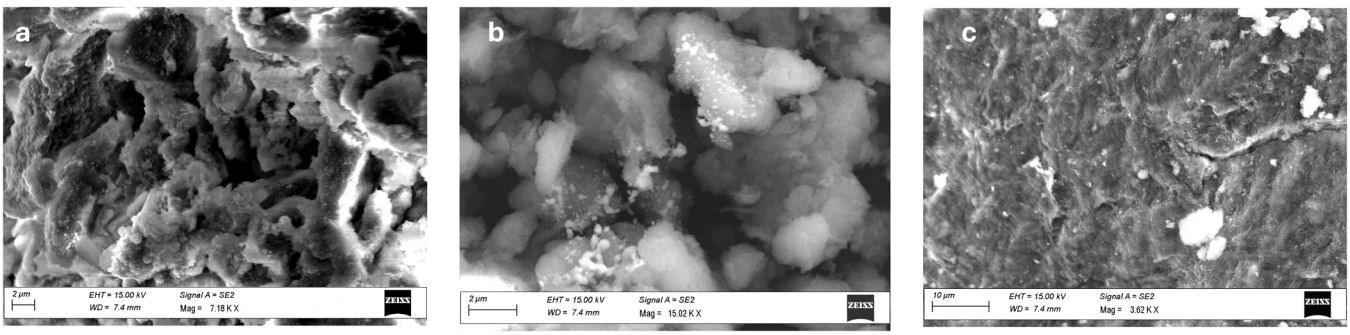

Fig. 7. SEM images of calcined $Ni/Ce/Al_2O_3$ (a), Ni/Ce/MK10 (b), and Ni/Ce/HDL (c) catalysts at 15.00Kv.

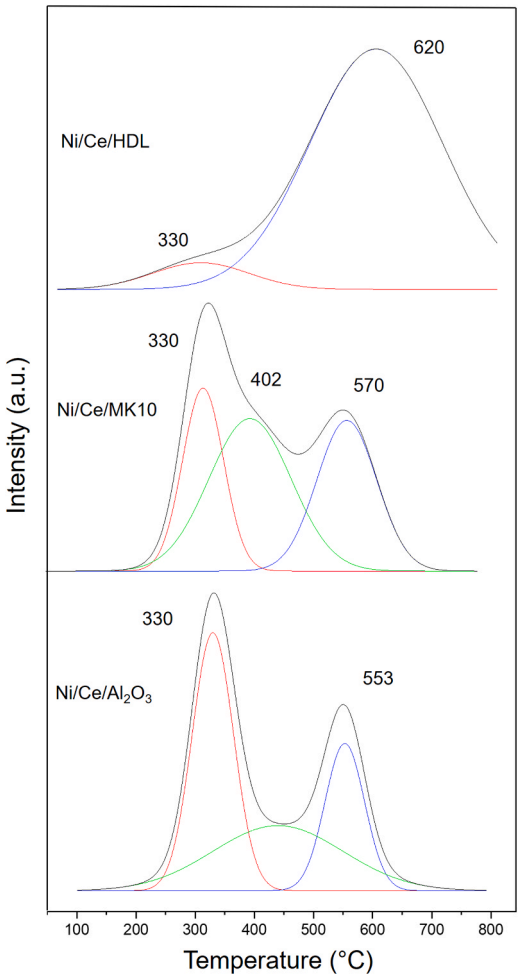

Fig. 8. TPR profiles for Ni/Ce/HDL, Ni/Ce/Al_2O_3 and Ni/Ce/MK10.

NiO.

The promoter effect on the catalysts was evaluated measuring their reducibility and basicity. The TPR plots are displayed in Fig. 8.

In the presence of cerium, the reducibility of nickel oxide seems modified. Comparing TPR profiles reported in Figs. 5 and 8, it is possible to observe that both Ni/Ce/Al_2O_3 and Ni/Ce/MK10 show the same reduction peak at 330 °C relative to the "crystallite NiO-like" of α-type, with an improving effect in the case of Ni/Al_2O_3 which increases part of its reducibility. Conversely, at higher temperatures, a different behavior was observed. Ni/Ce/Al_2O_3 also shows a reduction peak at 553 °C which is attributed to the reduction of Ni/Ce biphasic oxide, in which nickel species interact with the CeO_2 lattice [19]. Two reduction peaks are present in the case of Ni/Ce/MK10. One appears shifted towards a lower temperature (402 °C) with respect to the second peak revealed without promoter (439 °C), meaning that the Ni^{2+} species positioned in the octahedral alumina sites are not involved in a direct interaction with cerium oxide, but it is indirectly affected by its presence due to the variation of the chemical surroundings, as confirmed by XPS and the reduction appears facilitated. The second signal at 570 °C can be attributed to Ni/Ce biphasic oxide reduction, suggesting a better dispersion on the support of nickel and cerium oxides. The TPR analysis on the HDL-supported catalyst appears roughly similar to that in the absence of cerium oxide, confirming that the two oxides are deposited on two different areas of the support. XPS analyses performed on calcined Ni-Ce- samples highlight that in the case of Ni/Ce/Al_2O_3, Ni2$p_{3/2}$, and O1s spectra show only the typical peak components of bulk NiO, as evident from signal line-shape and BE values (Fig. S4) [71]. Also, the Ce signal is absent on the surface (Fig. S4), despite XPS

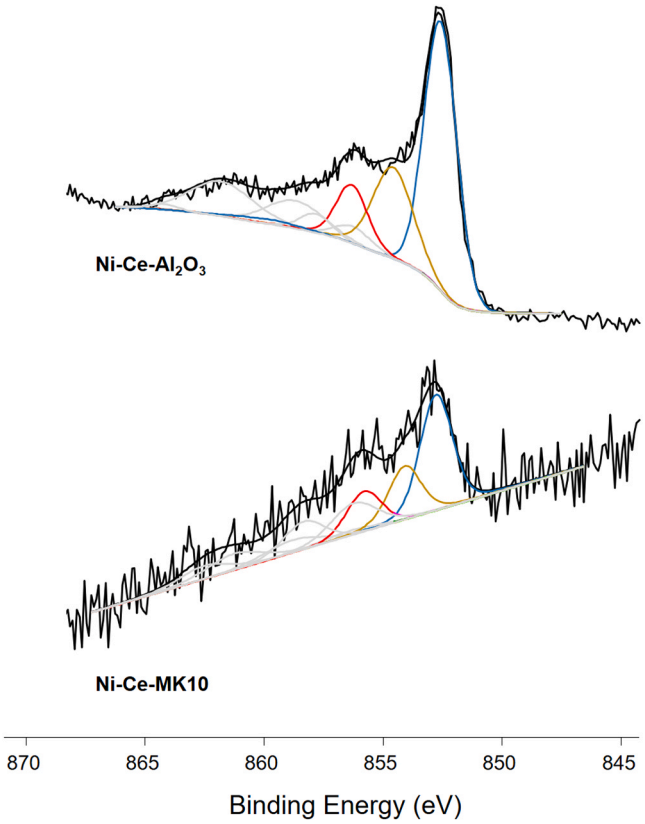

Fig. 9. Curve-fitted Ni2$p_{3/2}$ XP spectra of reduced Ni/Ce-catalysts. The multiplet splitting of the different Ni surface species is identified in the color code.

measurements before nickel loading, whereas EDX analyses on Ni/Ce/Al_2O_3 revealed its presence. This suggests that nickel deposition on alumina in the presence of the promoter leads to a preferential stratification of Ni species onto cerium ones. Differently, Ni2$p_{3/2}$ and O1s XP spectra of Ni/Ce/MK10 show peak components ascribable to Ni interaction with the support (Fig. S5).

In particular, we observed a single Nickel environment with the main peak at BE=856.9±0.1 eV, mainly attributable to Ni-silicate interaction (Ni-aluminate interaction if present is covered) [50,72,73]. Interestingly, the O1s spectral region evidenced a peak component at BE=530.2 ±0.1 eV, absent in Ni/Al_2O_3 and Ni/Ce/Al_2O_3, and compatible with Nickel oxides species affected by silicate environment. The same shift towards lower BE was observed for the Al2p peak as seen for the Ni/MK10 catalyst. Ce signals are detected, allowing us to hypothesize that Ni deposition leads preferentially this metal to interact with the support instead of Ce. After the reduction, Ni(0) is present on both the catalysts (Ni/Ce/Al_2O_3 and Ni/Ce/MK10), along with the other Ni chemical environments detected on the reduced Ni-supports surface (Fig. 9).

The Ni2$p_{3/2}$ curve fitting provided a relative abundance of the reduced Nickel species of 52±7 % for Ni/Ce/Al_2O_3 and 39±5 % for Ni/Ce/MK10. Although the XPS speciation analyses on the reduced samples revealed the presence of cerium exclusively as Ce(III), the TPR signals of cerium are not detected [74], probably due to their low quantity and are covered by those of nickel. It is worth mentioning that due to the synthetic procedure (SEA), the amount of cerium oxide present on the surface of the support is low (Table 4) and when MK10 is used, it is completely reduced to Ce(III). Interestingly, the most important effect of the cerium oxide addition was observed in the acid/base properties of the catalyst (Tables 2 and 5), especially in the case of Ni/Ce/MK10 in which the increase of basicity is much more evident with respect to the other systems. As was highlighted in Fig. 1 the presence of cerium oxide

increases the interaction of the catalyst with carbon dioxide. This was demonstrated through CO_2 adsorption/desorption analysis on MK10, Ni/MK10 and Ni/Ce/MK10. Table S2 and Fig. S6 summarize for comparison the CO_2-TPD analysis.

The cerium oxide loading not only increases the amount of adsorbed carbon dioxide improving the catalyst basicity but at the same time it favours the formation of medium-strength basic sites (480 °C desorption temperature, absent in the Ni/MK10 catalyst) that are traditionally the most active sites in the CO_2 methanation [75] increasing the carbon dioxide adsorption and its availability in the reaction with hydrogen over nickel.

4. Conclusions

In this study, a robust Ni(0)/Ce_2O_3/MK10 catalyst was prepared and successfully used in the methanation of carbon dioxide obtaining 76 % of CO_2 conversion with 100 % CH_4 selectivity at 260 °C after 3 h, remaining active at least for 5 cycles without reactivation requirement. Its catalytic activity and long lifetime were explained by correlation with textural and surface properties and compared with Ni/Ce catalysts supported on different aluminate and silicate-derived species. It was demonstrated that under low nickel and cerium loading conditions achieved through hydrothermal and impregnation, the correct ratio acidity/basicity, the best BET surface area and pore volume were obtained, a good metal center and promoter dispersion along the support allowing us to produce a very active and robust catalyst. We have also observed that less than 1 % cerium oxide increases the medium strength basic sites on the catalyst with a positive effect on CO_2 activation.

Funding

PON R&I 2014–2020 - ARS01_00868 and Progetto Competitivo MIUR CMPT222955 are gratefully acknowledged for financial support.

CRediT authorship contribution statement

Angela Dibenedetto: Writing – review & editing, Supervision, Project administration, Funding acquisition, Conceptualization. **Francesco Nocito:** Writing – original draft, Methodology, Investigation, Data curation. **Nicoletta Ditaranto:** Formal analysis.

Declaration of Competing Interest

No conflict of interest to declare.

Appendix A. Supporting information

Supplementary data associated with this article can be found in the online version at doi:10.1016/j.jcou.2024.102962.

Data availability

Data will be made available on request.

References

[1] A.N. Kay Lup, V. Soni, B. Keenan, J. Son, M.R. Taghartapeh, M.M. Morato, Y. Poya, R.M. Montañés, Sustainable energy technologies for the global south: challenges and solutions toward achieving SDG 7, Environ. Sci. Adv. 2 (2023) 570–585, https://doi.org/10.1039/D2VA00247G.

[2] F. Nocito, A. Dibenedetto, Atmospheric CO_2 mitigation technologies: carbon capture utilization and storage, Curr. Opin. Green Sustain. Chem. 21 (2020) 34–43, https://doi.org/10.1016/J.COGSC.2019.10.002.

[3] S. Li, S. Haussener, Design and operational guidelines of solar-driven catalytic conversion of CO_2 and H_2 to fuels, Appl. Energy 334 (2023) 120617, https://doi.org/10.1016/J.APENERGY.2022.120617.

[4] S. Bhattacharjee, M. Rahaman, V. Andrei, M. Miller, S. Rodríguez-Jiménez, E. Lam, C. Pornrungroj, E. Reisner, Photoelectrochemical CO_2-to-fuel conversion with simultaneous plastic reforming, Nat. Synth. 2 (2023) 182–192, https://doi.org/10.1038/s44160-022-00196-0.

[5] J. Mertens, C. Breyer, K. Arning, A. Bardow, R. Belmans, A. Dibenedetto, S. Erkman, J. Gripekoven, G. Goire Lé, S. Nizou, D. Pant, A.S. Reis-Machado, P. Styring, J. Vente, M. Webber, C. Lia, J. Sapart, Carbon capture and utilization: more than hiding CO_2 for some time, Joule 7 (2023) 431–449, https://doi.org/10.1016/j.joule.2023.01.005.

[6] A. Dibenedetto, F. Nocito, The future of carbon dioxide chemistry, ChemSusChem 13 (2020) 6219–6228, https://doi.org/10.1002/cssc.v13.23.

[7] P. Nikolaidis, A. Poullikkas, A comparative overview of hydrogen production processes, Renew. Sustain. Energy Rev. 67 (2017) 597–611, https://doi.org/10.1016/J.RSER.2016.09.044.

[8] J.M.F. Mendoza, D. Ibarra, Technology-enabled circular business models for the hybridisation of wind farms: integrated wind and solar energy, power-to-gas and power-to-liquid systems, Sustain. Prod. Consum. 36 (2023) 308–327, https://doi.org/10.1016/J.SPC.2023.01.011.

[9] W. Wang, J. Gong, Methanation of carbon dioxide: an overview, Front. Chem. Eng. China 5 (2011) 2–10, https://doi.org/10.1007/s11705-010-0528-3.

[10] J. Chen, Y. Zha, B. Liu, Y. Li, Y. Xu, X. Liu, Rationally designed water enriched nano reactor for stable CO_2 hydrogenation with near 100% ethanol selectivity over diatomic palladium active sites, ACS Catal. (2023) 7110–7121, https://doi.org/10.1021/ACSCATAL.3C00586/SUPPL_FILE/CS3C00586_SI_001.PDF.

[11] T. Tanabe, Y. Nagai, K. Dohmae, H. Sobukawa, H. Shinjoh, Sintering and redispersion behavior of Pt on Pt/MgO, J. Catal. 257 (2008) 117–124, https://doi.org/10.1016/J.JCAT.2008.04.012.

[12] A. Aitbekova, L. Wu, C.J. Wrasman, A. Boubnov, A.S. Hoffman, E.D. Goodman, S. R. Bare, M. Cargnello, Low-temperature restructuring of CeO_2-supported Ru nanoparticles determines selectivity in CO_2 catalytic reduction, J. Am. Chem. Soc. 140 (2018) 13736–13745, https://doi.org/10.1021/JACS.8B07615/SUPPL_FILE/JA8B07615_SI_001.PDF.

[13] K. Stangeland, D.Y. Kalai, H. Li, Z. Yu, Active and stable Ni based catalysts and processes for biogas upgrading: the effect of temperature and initial methane concentration on CO2 methanation, Appl. Energy 227 (2018) 206–212, https://doi.org/10.1016/J.APENERGY.2017.08.080.

[14] S. Ewald, M. Kolbeck, T. Kratky, M. Wolf, O. Hinrichsen, On the deactivation of Ni-Al catalysts in CO_2 methanation, Appl. Catal. A Gen. 570 (2019) 376–386, https://doi.org/10.1016/J.APCATA.2018.10.033.

[15] J. Barrientos, M. Lualdi, M. Boutonnet, S. Järås, Deactivation of supported nickel catalysts during CO methanation, Appl. Catal. A Gen. 486 (2014) 143–149, https://doi.org/10.1016/J.APCATA.2014.08.021.

[16] M. Zhang, X. Han, Y. Zeng, C. Charles Xu, Catalyst deactivation during hydrodeoxygenation reactions. Advances in Hydrotreating for Integrated Biofuel Production, 2024, pp. 233–249, 10.1016/B978-0-443-19076-6.00015-7.

[17] J. Sehested, J.A.P. Gelten, S. Helveg, Sintering of nickel catalysts: effects of time, atmosphere, temperature, nickel-carrier interactions, and dopants, Appl. Catal. A Gen. 309 (2006) 237–246, https://doi.org/10.1016/J.APCATA.2006.05.017.

[18] Z. Zhang, Y. Tian, L. Zhang, S. Hu, J. Xiang, Y. Wang, L. Xu, Q. Liu, S. Zhang, X. Hu, Impacts of nickel loading on properties, catalytic behaviors of Ni/γ–Al_2O_3 catalysts and the reaction intermediates formed in methanation of CO_2, Int. J. Hydrog. Energy 44 (2019) 9291–9306, https://doi.org/10.1016/J.IJHYDENE.2019.02.129.

[19] C. Sun, P. Beaunier, P. Da Costa, Effect of ceria promotion on the catalytic performance of Ni/SBA-16 catalysts for CO_2 methanation, Catal. Sci. Technol. 10 (2020) 6330–6341, https://doi.org/10.1039/d0cy00922a.

[20] J. Ren, X. Qin, J.Z. Yang, Z.F. Qin, H.L. Guo, J.Y. Lin, Z. Li, Methanation of carbon dioxide over Ni–M/ZrO2 (M = Fe, Co, Cu) catalysts: effect of addition of a second metal, Fuel Process. Technol. 137 (2015) 204–211, https://doi.org/10.1016/J.FUPROC.2015.04.022.

[21] P. Riani, E. Spennati, M.V. Garcia, V.S. Escribano, G. Busca, G. Garbarino, Ni/Al2O3 catalysts for CO_2 methanation: effect of silica and nickel loading, Int. J. Hydrog. Energy 48 (2023) 24976–24995, https://doi.org/10.1016/J.IJHYDENE.2023.01.002.

[22] F. Wang, X. Tian, Y. Shi, W. Fan, Q. Liu, Photocatalytic CO_2 methanation over the Ni/SiO_2 catalysts for performance enhancement, Int. J. Hydrog. Energy 68 (2024) 1382–1392, https://doi.org/10.1016/J.IJHYDENE.2024.04.350.

[23] M. Li, H. Amari, A.C. van Veen, Metal-oxide interaction enhanced CO_2 activation in methanation over ceria supported nickel nanocrystallites, Appl. Catal. B Environ. 239 (2018) 27–35, https://doi.org/10.1016/J.APCATB.2018.07.074.

[24] G. De Piano, J.J. Andrade Gamboa, A.M. Condó, F.C. Gennari, CO_2 methanation over nickel-CeO_2 catalyst supported on Al_2O_3: different impregnation strategies and Ni-Ce ratios, Int. J. Hydrog. Energy 56 (2024) 1007–1019, https://doi.org/10.1016/J.IJHYDENE.2023.12.255.

[25] J. Ma, Q. Jiang, S. Li, W. Chu, H. Qian, S. Perathoner, G. Centi, Y. Liu, High-dispersed CeOx species on mesopores silica to accelerate Ni-catalysed CO_2 methanation at low temperatures, Chem. Eng. J. 479 (2024) 147453, https://doi.org/10.1016/J.CEJ.2023.147453.

[26] Y.R. Dias, O.W. Perez-Lopez, CO_2 methanation over Ni-Al LDH-derived catalyst with variable Ni/Al ratio, J. CO_2 Util. 68 (2023) 102381, https://doi.org/10.1016/j.jcou.2022.102381.

[27] S. Lin, R. Tang, X. Liu, L. Gong, Z. Li, Modulating CO_2 methanation activity on Ni/CeO_2 catalysts by tuning ceria facet-induced metal-support interaction, Int. J. Hydrog. Energy 51 (2024) 462–475, https://doi.org/10.1016/J.IJHYDENE.2023.10.095.

[28] P. Völs, B. Störr, A. Lißner, F. Mertens, A comparative study on the influence of potential 4th period promoters in Ni-bimetallic catalysts for CO_2 methanation, Fuel 358 (2024) 130141, https://doi.org/10.1016/J.FUEL.2023.130141.

[29] N.P. Nguyen, B.N.T. Le, T. Nguyen, T.L.H. Duong, H.H.T. Nguyen, D.V.N. Vo, T. T. Nguyen, H.D.P. Nguyen, T.P.T. Pham, Nickel catalyst supported on SiC incorporated SiO_2 for CO_2 methanation: positive effects of dysprosium promoter and microwaves heating method, Fuel 363 (2024) 130939, https://doi.org/10.1016/J.FUEL.2024.130939.

[30] A. Alarcón, J. Guilera, J.A. Díaz, T. Andreu, Optimization of nickel and ceria catalyst content for synthetic natural gas production through CO_2 methanation, Fuel Process. Technol. 193 (2019) 114–122, https://doi.org/10.1016/J.FUPROC.2019.05.008.

[31] L. Zhou, Q. Wang, L. Ma, J. Chen, J. Ma, Z. Zi, CeO_2 Promoted mesoporous Ni/γ-Al_2O_3 catalyst and its reaction conditions for CO_2 methanation, Catal. Lett. 145 (2015) 612–619, https://doi.org/10.1007/S10562-014-1426-Y/FIGURES/9.

[32] H. Liu, X. Zou, X. Wang, X. Lu, W. Ding, Effect of CeO_2 addition on Ni/Al_2O_3 catalysts for methanation of carbon dioxide with hydrogen, J. Nat. Gas Chem. 21 (2012) 703–707, https://doi.org/10.1016/S1003-9953(11)60422-2.

[33] S.M. Ahmed, J. Ren, I. Ullah, H. Lou, N. Xu, Z. Abbasi, Z. Wang, Ni-based catalysts for CO2 methanation: exploring the support role in structure-activity relationships, ChemSusChem (2024), https://doi.org/10.1002/cssc.202400310.

[34] C. Shen, C. Liu, CO_2 Methanation over the supported Ni catalysts, Struct. Eff. (2024) 105–114, https://doi.org/10.1007/978-981-99-8822-8_5.

[35] G. Busca, E. Spennati, P. Riani, G. Garbarino, mechanistic and compositional aspects of industrial catalysts for selective CO_2 hydrogenation processes, Catalysts 14 (14) (2024) 95, https://doi.org/10.3390/CATAL14020095.

[36] H. Zhao, C.H. Zhou, L.M. Wu, J.Y. Lou, N. Li, H.M. Yang, D.S. Tong, W.H. Yu, Catalytic dehydration of glycerol to acrolein over sulfuric acid-activated montmorillonite catalysts, Appl. Clay Sci. 74 (2013) 154–162, https://doi.org/10.1016/J.CLAY.2012.09.011.

[37] B.S. Kumar, A. Dhakshinamoorthy, K. Pitchumani, K10 montmorillonite clays as environmentally benign catalysts for organic reactions, Catal. Sci. Technol. 4 (2014) 2378–2396, https://doi.org/10.1039/C4CY00112E.

[38] M.G. Clerici, G. Bellussi, U. Romano, Synthesis of propylene oxide from propylene and hydrogen peroxide catalyzed by titanium silicalite, J. Catal. 129 (1991) 159–167, https://doi.org/10.1016/0021-9517(91)90019-Z.

[39] O.M. Perrone, F. Lobefaro, M. Aresta, F. Nocito, M. Boscolo, A. Dibenedetto, Butanol synthesis from ethanol over CuMgAl mixed oxides modified with palladium (II) and indium (III), Fuel Process. Technol. 177 (2018) 353–357, https://doi.org/10.1016/J.FUPROC.2018.05.006.

[40] M. Ventura, F. Lobefaro, E. de Giglio, M. Distaso, F. Nocito, A. Dibenedetto, Selective aerobic oxidation of 5-Hydroxymethylfurfural to 2,5-Diformylfuran or 2-Formyl-5-furancarboxylic acid in water by using MgO·CeO_2 mixed oxides as catalysts, ChemSusChem 11 (2018) 1305–1315, https://doi.org/10.1002/CSSC.201800334.

[41] J.A. Schwarz, C. Contescu, A. Contescu, Methods for preparation of catalytic materials, Chem. Rev. 95 (1995) 477–510, https://doi.org/10.1021/CR00035A002/ASSET/CR00035A002.FP.PNG_V03.

[42] Y. Kim, S. Kwon, Y. Song, K. Na, Catalytic CO_2 hydrogenation using mesoporous bimetallic spinel oxides as active heterogeneous base catalysts with long lifetime, J. CO_2 Util. 36 (2020) 145–152, https://doi.org/10.1016/j.jcou.2019.11.005.

[43] Z.X. Sun, T.T. Zheng, Q.B. Bo, M. Du, W. Forsling, Effects of calcination temperature on the pore size and wall crystalline structure of mesoporous alumina, J. Colloid Interface Sci. 319 (2008) 247–251, https://doi.org/10.1016/J.JCIS.2007.11.023.

[44] F. Meng, Z. Li, J. Liu, X. Cui, H. Zheng, Effect of promoter Ce on the structure and catalytic performance of Ni/Al_2O_3 catalyst for CO methanation in slurry-bed reactor, J. Nat. Gas Sci. Eng. 23 (2015) 250–258, https://doi.org/10.1016/J.JNGSE.2015.01.041.

[45] W. Gac, W. Zawadzki, M. Rotko, M. Greluk, G. Słowik, G. Kolb, Effects of support composition on the performance of nickel catalysts in CO_2 methanation reaction, Catal. Today 357 (2020) 468–482, https://doi.org/10.1016/J.CATTOD.2019.07.026.

[46] H.M. Gobara, S.A. Hassan, A comparative study of surface characteristics of nickel supported on silica gel, γ-alumina, aluminosilicate, Pet. Sci. Technol. 27 (2009) 1555–1571, https://doi.org/10.1080/10916460802608677.

[47] M.C. Biesinger, B.P. Payne, L.W.M. Lau, A. Gerson, R.S.C. Smart, X-ray photoelectron spectroscopic chemical state quantification of mixed nickel metal, oxide and hydroxide systems, Surf. Interface Anal. 41 (2009) 324–332, https://doi.org/10.1002/sia.3026.

[48] Chung Ping Li, A. Proctor, D.M. Hercules, Curve fitting analysis of ESCA Ni 2p spectra of Nickel-Oxygen compounds and Ni/Al_2O_3 catalysts, Appl. Spectrosc. 38 (1984) 880–886, https://doi.org/10.1366/0003702844554530.

[49] G. Li, L. Hu, J.M. Hill, Comparison of reducibility and stability of alumina-supported Ni catalysts prepared by impregnation and co-precipitation, Appl. Catal. A Gen. 301 (2006) 16–24, https://doi.org/10.1016/J.APCATA.2005.11.013.

[50] A.M. Venezia, R. Bertoncello, G. Deganello, X-ray photoelectron spectroscopy investigation of pumice-supported nickel catalysts, Surf. Interface Anal. 23 (1995) 239–247, https://doi.org/10.1002/sia.740230408.

[51] T. Asakawa, K. Tanaka, I. Toyoshima, Interaction of Ni with SiOx or SiO_2 formed on Si(111) and co adsorption inhibition in Ni/SiOx/n-Si(111) studied by XPS and AES, Langmuir 4 (1988) 521–526, https://doi.org/10.1021/la00081a005.

[52] M.Lo Jacono, M. Schiavello, A. Cimino, Structural, magnetic, and optical properties of nickel oxide supported on eta and γ-aluminas, J. Phys. Chem. 75 (1971) 1044–1050, https://doi.org/10.1021/J100678A005/ASSET/J100678A005.FP.PNG_V03.

[53] A. Zhao, W. Ying, H. Zhang, H. Ma, D. Fang, Ni-Al_2O_3 catalysts prepared by solution combustion method for syngas methanation, Catal. Commun. 17 (2012) 34–38, https://doi.org/10.1016/j.catcom.2011.10.010.

[54] B. Mile, D. Stirling, M.A. Zammitt, A. Lovell, M. Webb, The location of nickel oxide and nickel in silica-supported catalysts: two forms of "NiO" and the assignment of temperature-programmed reduction profiles, J. Catal. 114 (1988) 217–229, https://doi.org/10.1016/0021-9517(88)90026-7.

[55] W. Shan, M. Luo, P. Ying, W. Shen, C. Li, Reduction property and catalytic activity of $Ce_{1-x}Ni_xO_2$ mixed oxide catalysts for CH_4 oxidation, Appl. Catal. A Gen. 246 (2003) 1–9, https://doi.org/10.1016/S0926-860X(02)00659-2.

[56] G. Poncelet, M.A. Centeno, R. Molina, Characterization of reduced α-alumina-supported nickel catalysts by spectroscopic and chemisorption measurements, Appl. Catal. A Gen. 288 (2005) 232–242, https://doi.org/10.1016/J.APCATA.2005.04.052.

[57] P. Kim, Y. Kim, H. Kim, I.K. Song, J. Yi, Synthesis and characterization of mesoporous alumina with nickel incorporated for use in the partial oxidation of methane into synthesis gas, Appl. Catal. A Gen. 272 (2004) 157–166, https://doi.org/10.1016/J.APCATA.2004.05.055.

[58] N.W. Hurst, S.J. Gentry, A. Jones, Temperature programmed reduction, Catal. Rev. Sci. Eng. 24 (1982) 233–309, https://doi.org/10.1080/03602458208079654.

[59] S. Valinejad Moghaddam, M. Rezaei, F. Meshkani, R. Daroughegi, Carbon dioxide methanation over Ni-M/Al_2O_3 (M: Fe, CO, Zr, La and Cu) catalysts synthesized using the one-pot sol-gel synthesis method, Int. J. Hydrog. Energy 43 (2018) 16522–16533, https://doi.org/10.1016/J.IJHYDENE.2018.07.013.

[60] P. Summa, B. Samojeden, M. Motak, D. Wierzbicki, I. Alxneit, K. Świerczek, P. Da Costa, Investigation of Cu promotion effect on hydrotalcite-based nickel catalyst for CO_2 methanation, Catal. Today 384–386 (2022) 133–145, https://doi.org/10.1016/J.CATTOD.2021.05.004.

[61] P. Frontera, A. Macario, M. Ferraro, P. Antonucci, B. Louis, Q. Wang, M.M. Pereira, Supported catalysts for CO_2 methanation: a review, Catalysts 7 (2017) (2017) 59, https://doi.org/10.3390/CATAL7020059.

[62] L. Xu, F. Wang, M. Chen, D. Nie, X. Lian, Z. Lu, H. Chen, K. Zhang, P. Ge, CO_2 methanation over rare earth doped Ni based mesoporous catalysts with intensified low-temperature activity, Int. J. Hydrog. Energy 42 (2017) 15523–15539, https://doi.org/10.1016/J.IJHYDENE.2017.05.027.

[63] G. Zhou, H. Liu, K. Cui, A. Jia, G. Hu, Z. Jiao, Y. Liu, X. Zhang, Role of surface Ni and Ce species of Ni/CeO_2 catalyst in CO_2 methanation, Appl. Surf. Sci. 383 (2016) 248–252, https://doi.org/10.1016/J.APSUSC.2016.04.180.

[64] W.K. Fan, M. Tahir, Recent trends in developments of active metals and heterogenous materials for catalytic CO_2 hydrogenation to renewable methane: a review, J. Environ. Chem. Eng. 9 (2021) 105460, https://doi.org/10.1016/J.JECE.2021.105460.

[65] A.I. Tsiotsias, N.D. Charisiou, A. AlKhoori, S. Gaber, V. Stolojan, V. Sebastian, B. van der Linden, A. Bansode, S.J. Hinder, M.A. Baker, K. Polychronopoulou, M. A. Goula, Optimizing the oxide support composition in Pr-doped CeO_2 towards highly active and selective Ni-based CO_2 methanation catalysts, J. Energy Chem. 71 (2022) 547–561, https://doi.org/10.1016/J.JECHEM.2022.04.003.

[66] A.A. Alkhoori, O. Elmutasim, A.A. Dabbawala, M.A. Vasiliades, K.C. Petallidou, A. H. Emwas, D.H. Anjum, N. Singh, M.A. Baker, N.D. Charisiou, M.A. Goula, A. M. Efstathiou, K. Polychronopoulou, mechanistic features of the CeO_2-modified Ni/Al_2O_3 catalysts for the CO_2 methanation reaction: experimental and Ab initio studies, ACS Appl. Energy Mater. 6 (2023) 8550–8571, https://doi.org/10.1021/ACSAEM.3C01437/SUPPL_FILE/AE3C01437_SI_001.PDF.

[67] A.A. Alkhoori, A.A. Dabbawala, M.A. Baker, S. Mao, N. Charisiou, S.S. Hinder, M. Harfouche, D.H. Anjum, M.A. Goula, K. Polychronopoulou, From earth material to energy production: Ni-based modified halloysite catalysts for CO_2 methanation, Appl. Clay Sci. 259 (2024) 107514, https://doi.org/10.1016/J.CLAY.2024.107514.

[68] C. Sun, P. Beaunier, P. Da Costa, Effect of ceria promotion on the catalytic performance of Ni/SBA-16 catalysts for CO_2 methanation, Catal. Sci. Technol. 10 (2020) 6330–6341, https://doi.org/10.1039/D0CY00922A.

[69] S. Singha, M. Sahoo, K.M. Parida, Chemoselective oxidation of primary alcohols catalysed by Ce(III)-complex intercalated LDH using molecular oxygen at room temperature, Dalton Trans. 40 (2011) 11838–11844, https://doi.org/10.1039/C1DT11140J.

[70] M. Rahromostaqim, M. Sahimi, Molecular dynamics study of the effect of layer charge and interlayer cations on swelling of mixed-layer chlorite-montmorillonite clays, J. Phys. Chem. C 124 (2020) 2553–2561, https://doi.org/10.1021/ACS.JPCC.9B10919/ASSET/IMAGES/MEDIUM/JP9B10919_0010.GIF.

[71] J.F. Moulder, W.F. Stickle, P.E. Sobol, K.D. Bomben, Handbook of X-ray Photoelectron Spectroscopy, Physical Electronics Inc, Eden Prairie, Minnesota, 1992.

[72] J.P. Espinós, A.R. Gonzalez-Elipe, A. Caballero, J. García, G. Munuera, The state of nickel in Ni/SiO_2 and Ni/TiO_2-calcined catalysts, J. Catal. 136 (1992) 415–422, https://doi.org/10.1016/0021-9517(92)90072-P.

[73] R.B. Shalvoy, P.J. Reucroft, B.H. Davis, Characterization of coprecipitated nickel on silica methanation catalysts by X-ray photoelectron spectroscopy, J. Catal. 56 (1979) 336–348, https://doi.org/10.1016/0021-9517(79)90126-X.

[74] S. Zhang, S. Muratsugu, N. Ishiguro, M. Tada, Ceria-doped Ni/SBA-16 catalysts for dry reforming of methane, ACS Catal. 3 (2013) 1855–1864, https://doi.org/10.1021/CS400159W/SUPPL_FILE/CS400159W_SI_001.PDF.

[75] Q. Pan, J. Peng, T. Sun, S. Wang, S. Wang, Insight into the reaction route of CO_2 methanation: promotion effect of medium basic sites, Catal. Commun. 45 (2014) 74–78, https://doi.org/10.1016/J.CATCOM.2013.10.034.